

Spatial entanglement patterns and Einstein-Podolsky-Rosen steering in a Bose-Einstein condensate

Matteo Fadel, Tilman Zibold, Boris Décamps, Philipp Treutlein*

Department of Physics, University of Basel,
Klingelbergstrasse 82, 4056 Basel, Switzerland

*To whom correspondence should be addressed; E-mail: philipp.treutlein@unibas.ch

Many-particle entanglement is a fundamental concept of quantum physics that still presents conceptual challenges. While spin-squeezed and other non-classical states of atomic ensembles were used to enhance measurement precision in quantum metrology, the notion of entanglement in these systems remained controversial because the correlations between the indistinguishable atoms were witnessed by collective measurements only. Here we use high-resolution imaging to directly measure the spin correlations between spatially separated parts of a spin-squeezed Bose-Einstein condensate. We observe entanglement that is strong enough for Einstein-Podolsky-Rosen steering: we can predict measurement outcomes for non-commuting observables in one spatial region based on a corresponding measurement in another region with an inferred uncertainty product below the Heisenberg relation. This could be exploited for entanglement-enhanced imaging of electromagnetic field distributions and quantum information tasks beyond metrology.

Two quantum mechanical degrees of freedom are entangled (nonseparable) if the quantum state of one cannot be described independently of the other. When measurements are performed on both, entanglement results in correlations between the outcomes. While entanglement can exist between any quantum degrees of freedom, the conflict with classical physics is particularly striking when the correlations are observed between measurement outcomes obtained in spatially separated regions. Einstein, Podolsky and Rosen pointed out [1] that if the correlations are sufficiently strong, local measurements in one region A can apparently change the quantum state in a spatially separated region B , a scenario Schrödinger named “steering” [2]. The possibility of steering between spatially separated systems implies that quantum theory is in conflict with a local realist description of the world [3]. In fact, steering allows an observer in A to use her local measurement outcomes to predict the outcomes of non-commuting measurements in B with uncertainties below the Heisenberg uncertainty relation for B . EPR steering has been extensively explored with optical systems[3]. Between spatially separated atomic ensembles, entanglement was observed [4, 5, 6, 7], but EPR steering has not yet been achieved for more than two atoms [8]. Demonstrating the EPR paradox with ensembles of massive particles is desirable as it puts quantum physics to a stringent test in a new regime of increasingly macroscopic systems [3].

Experiments with ultracold atomic ensembles recently made rapid progress and a variety of nonclassical states can be prepared [9]. Besides being of fundamental interest, such states find applications in quantum metrology [10], where the correlations between the constituent atoms are exploited to reduce the noise in atom interferometric measurements [11, 12, 13, 14]. Because of the large number of atoms involved, it is usually not possible to address and detect the atoms individually. In the case of Bose-Einstein condensates (BECs), it is even impossible in principle: the atoms are identical particles that occupy the same spatial mode. Still, quantum correlations between them can be characterized with the help of witness observables

that involve only collective measurements on the entire ensemble [15, 16]. This approach has been used to reveal the presence of entanglement[11, 17], EPR correlations[18], and even Bell correlations[19] in a cloud of atoms. However, these non-classical correlations have not yet been observed directly by performing measurements on spatially separated subsystems. Moreover, many authors have questioned whether the concept of entanglement in systems of indistinguishable particles is fully legitimate and useful for tasks other than metrology ¹.

As pointed out in the theoretical work of Killoran *et al.* [20], the presence of entanglement in an ensemble of indistinguishable particles can be unambiguously confirmed by extracting it into spatially separated modes, turning it into a resource for a variety of quantum information tasks.

In our experiment, we demonstrate that entanglement can be extracted from spatially separated parts of a spin-squeezed BEC and use it to demonstrate the EPR paradox with an atomic system.

The quantum degrees of freedom in our experiment are two collective spins [9] \hat{S}^A and \hat{S}^B that describe the internal state of atoms in regions A and B , respectively. Each atom is an effective two-level system with internal states $|1\rangle$ and $|2\rangle$. The component $\hat{S}_z^A = (\hat{N}_1^A - \hat{N}_2^A)/2$ is half the atom number difference between the states, evaluated in region A , and a similar definition holds for \hat{S}_z^B . Other spin components can be measured by applying appropriate spin rotations before detection. To detect entanglement we use the criterion of Giovannetti *et al.* [21], who have shown that for all separable states

$$\mathcal{E}_{\text{Ent}} = \frac{4 \text{Var}(g_z \hat{S}_z^A + \hat{S}_z^B) \text{Var}(g_y \hat{S}_y^A + \hat{S}_y^B)}{\left(|g_z g_y| |\langle \hat{S}_x^A \rangle| + |\langle \hat{S}_x^B \rangle|\right)^2} \geq 1, \quad (1)$$

where $\text{Var}(\cdot)$ denotes the variance and g_z, g_y , are real parameters that can be optimized to minimize \mathcal{E}_{Ent} . Therefore, $\mathcal{E}_{\text{Ent}} < 1$ is a sufficient condition to certify entanglement (nonseparability)

¹For a brief review of the debate, see [20].

between A and B . The variances in Eq. (1) quantify the uncertainty with which an observer in A can predict (infer) the outcome of a spin measurement in B , based on a measurement on her own system, and are therefore called inferred variances.

If correlations between A and B are strong enough, an observer in A can predict the result of non-commuting measurements performed by B with a product of the inferred variances below the Heisenberg uncertainty bound for system B , *i.e.* there is a violation of the relation [3]

$$\mathcal{E}_{\text{EPR}}^{A \rightarrow B} = \frac{4 \text{Var}(g_z \hat{S}_z^A + \hat{S}_z^B) \text{Var}(g_y \hat{S}_y^A + \hat{S}_y^B)}{|\langle \hat{S}_x^B \rangle|^2} \geq 1. \quad (2)$$

Note that if there are no correlations between A and B , the variances in Eq. (2) are minimized for $g_z = g_y = 0$, for which the spin uncertainty relation for B is recovered. In the presence of a violation of Eq. (2), B must conclude that he is in the paradoxical situation considered by EPR, where A is able to predict his measurement results without any classical communication. Note that a violation of Eq. (1) does not imply a violation of Eq. (2), while the converse is true. This reflects the fact that entanglement is necessary but not sufficient for EPR steering, and that they are inequivalent types of correlations [22, 23]. Moreover, the asymmetry between A and B present in Eq. (2) implies that if A can steer B (denoted $A \rightarrow B$), then not necessarily B can steer A ($B \rightarrow A$), as investigated both theoretically [24] and experimentally [25] in optics.

To demonstrate a violation of both Eq. (1) and Eq. (2) with a massive many-particle system, we perform experiments with two-component BECs of $N = 530 \pm 40$ ^{87}Rb atoms, magnetically trapped on an atom chip [26]. The two components correspond to the hyperfine states $|F = 1, m_F = -1\rangle \equiv |1\rangle$ and $|F = 2, m_F = 1\rangle \equiv |2\rangle$ and occupy nearly identical spatial modes. They can be described by a collective spin \hat{S} , referring to the entire BEC. We prepare the BEC in a spin-squeezed state by controlling atomic collisions with a state-dependent potential, as described in ref. [19, 17, 14]. The spin-squeezed state features quantum correlations between the atoms, which reduce fluctuations of \hat{S}_z and increase fluctuations of \hat{S}_y while

maintaining a large spin polarization in \hat{S}_x (see Fig. 1b). We obtain typically $-3.2(2)$ dB of spin squeezing according to the Wineland criterion [27]. Alternatively, we can prepare the BEC in a coherent spin state, where the atomic internal states are uncorrelated.

In order to access spatially separated regions in the BEC, we use the sequence illustrated in Fig. 1a. After preparing the state, the atomic cloud is released from the trap and expands during a 2.2 ms time-of-flight. This expansion is spin-independent since collisional interactions are very similar for $|1\rangle$ and $|2\rangle$ and leads to a magnification of the atomic cloud without affecting the spin correlations between the atoms.

Next, we set the axis \vec{n} of the spin components \hat{S}_n^A and \hat{S}_n^B to be measured by applying a Rabi rotation pulse to the entire atomic cloud. Immediately thereafter, we record two high-resolution absorption images [28] of the atomic density distributions in states $|2\rangle$ and $|1\rangle$ by illuminating the atomic cloud twice with a resonant laser beam. The imaging pulses project the spin state and simultaneously localize the atoms in well-defined positions. Fig. 1c shows typical absorption images taken in this way. This experimental sequence is repeated hundreds of times, alternating the measurement direction \vec{n} along either x , y or z .

We now define the two regions A and B to be analyzed on all pairs of absorption images (Fig. 1c). Counting the atom numbers N_1^A and N_2^A in region A realizes a single-shot projective measurement of the local collective spin $\hat{S}_n^A = (N_1^A - N_2^A)/2$. The same approach is applied to region B , which yields \hat{S}_n^B . The spins \hat{S}_n^A and \hat{S}_n^B are well defined if the atomic densities can be unambiguously attributed to the corresponding region on the absorption image. The finite optical resolution, in combination with a redistribution of atomic density due to the random photon scattering during imaging, amounts to an uncertainty in the atomic position of $\sigma_{\text{blur}} = 1.8 \mu\text{m}$, corresponding to 1.4 pixels on the images. To minimize the effect of crosstalk between A and B , we leave a gap of 3 pixels between the two regions. In this way, on average less than four atoms are simultaneously detected in both regions, rendering crosstalk negligible

(Supplementary Materials).

To detect entanglement between regions A and B we evaluate Eq. (1) for different positions of the gap, corresponding to different splitting ratios $N^A/(N^A + N^B)$, where $N^A = N_1^A + N_2^A$ and similar for N^B (Fig. 2a, green dots). For a wide range of splitting ratios we observe a violation of the inequality in Eq. (1), which proves that the two local spins \hat{S}^A and \hat{S}^B are entangled. This extracted entanglement derives from the quantum correlations among the indistinguishable atoms in the initial state[20], since the expansion of the cloud, the spin rotation and detection do not create correlations. For comparison, the same analysis has also been applied to measurements performed on a coherent spin state, which does not show entanglement within the error bars (Fig. 2a, orange dots).

An intriguing feature of our approach to extract entanglement from a many-body state is that the subsystems can be defined a posteriori on the images. This is in contrast to other experiments where the subsystems are defined by the experimental setup [4, 5, 6, 7] or by the source of the state [3, 25]. We exploit this feature to detect entanglement between regions A and B patterned in a variety of different shapes, see Fig. 2b. The fact that we observe entanglement between all such regions reflects the symmetry of the underlying many-body quantum state: the quantum state of the indistinguishable bosons in the condensate has to be symmetric under particle exchange. Consequently, each atom is entangled with all other atoms, and the entanglement extends over the entire atomic cloud. For comparison, we again show measurements for a coherent spin state, which does not show entanglement.

The correlations in our system are strong enough to demonstrate an EPR paradox: Fig. 3a shows a measurement of the EPR criterion Eq. (2) for vertical splitting of the cloud and different positions of the gap. We observe EPR steering $A \rightarrow B$ (green data points), which is maximized for non-symmetric splitting. The asymmetry indicates the presence of technical noise [29]. For comparison, we evaluate the spin uncertainty relation $4 \text{Var}(\hat{S}_z^B) \text{Var}(\hat{S}_y^B)/|\langle \hat{S}_x^B \rangle|^2 \geq 1$ for

system B , illustrating the reduction of the uncertainty product when replacing the non-inferred variances with the inferred ones. As can be seen in Eq. (2), EPR steering is an asymmetric concept. By relabeling region A as B and vice versa, we can invert the roles of the steering and steered systems. This inverted scenario also shows EPR steering $B \rightarrow A$ (red data points in Fig. 3a). The absence of a splitting ratio showing two-way steering $A \leftrightarrow B$ indicates the presence of noise in our system [24, 25].

Finally, we characterize the robustness of the observed EPR steering $A \rightarrow B$ to a variation of the gap size. We fix the central position of the gap such that the splitting ratio is 0.77 (the ratio maximizing steering $A \rightarrow B$ in Fig. 3a) and change the gap width symmetrically with respect to this position (Fig. 3c). We observe that EPR steering vanishes for large widths of the gap, where the size of the steered system is considerably reduced (Fig. 3b).

We have shown that entanglement and EPR steering can be observed between the collective spins in different spatial regions of a many-body system. These results are based on the extraction of entanglement from a system of identical particles, and on the observation that local collective spins, associated with arbitrary patterns in the atomic density images, satisfy criteria certifying entanglement and EPR steering. Our method can be applied to quantum metrology, for example for the measurement of field distributions with an uncertainty beyond the standard quantum limit. Moreover, EPR entanglement is a resource for tasks such as quantum teleportation and quantum key distribution [3]. Furthermore, our study raises the question whether Bell correlations could also be observed between spatially separated regions, and if such correlations can be distributed over macroscopic distances by splitting the atomic cloud.

Complementary to our work, the group of M. Oberthaler has observed spatially distributed multipartite entanglement and the group of C. Klempt has detected entanglement of spatially separated modes.

References

- [1] A. Einstein, B. Podolsky, N. Rosen, *Physical Review* **47**, 777 (1935).
- [2] E. Schrödinger, *Proceedings of the Cambridge Philosophical Society* **31**, 555 (1935).
- [3] M. D. Reid, *et al.*, *Rev. Mod. Phys.* **81**, 1727 (2009).
- [4] B. Julsgaard, A. Kozhekin, E. S. Polzik, *Nature* **413**, 400 (2001).
- [5] C. W. Chou, *et al.*, *Nature* **438**, 828 (2005).
- [6] D. N. Matsukevich, *et al.*, *Physical Review Letters* **96**, 030405 (2006).
- [7] J. Simon, H. Tanji, S. Ghosh, V. Vuletic, *Nature Physics* **3**, 765 (2007).
- [8] E. Hagley, *et al.*, *Physical Review Letters* **79**, 1 (1997).
- [9] L. Pezzé, A. Smerzi, M. K. Oberthaler, R. Schmied, P. Treutlein, Non-classical states of atomic ensembles: fundamentals and applications in quantum metrology (2016).
- [10] V. Giovannetti, S. Lloyd, L. Maccone, *Nature Photonics* **5**, 222 (2011).
- [11] C. Gross, T. Zibold, E. Nicklas, J. Estève, M. K. Oberthaler, *Nature* **464**, 1165 (2010).
- [12] A. Louchet-Chauvet, *et al.*, *New Journal of Physics* **12**, 065032 (2010).
- [13] I. D. Leroux, M. H. Schleier-Smith, V. Vuletić, *Phys. Rev. Lett.* **104**, 250801 (2010).
- [14] C. F. Ockeloen, R. Schmied, M. F. Riedel, P. Treutlein, *Phys. Rev. Lett.* **111**, 143001 (2013).
- [15] L. Amico, R. Fazio, A. Osterloh, V. Vedral, *Rev. Mod. Phys.* **80**, 517 (2008).
- [16] O. Gühne, G. Tóth, *Physics Reports* **474**, 1 (2009).

- [17] M. F. Riedel, *et al.*, *Nature* **464**, 1170 (2010).
- [18] J. Peise, *et al.*, *Nature Communications* **6**, 8984 EP (2015).
- [19] R. Schmied, *et al.*, *Science* **352**, 441 (2016).
- [20] N. Killoran, M. Cramer, M. B. Plenio, *Physical Review Letters* **112**, 150501 (2014).
- [21] V. Giovannetti, S. Mancini, D. Vitali, P. Tombesi, *Phys. Rev. A* **67**, 022320 (2003).
- [22] H. M. Wiseman, S. J. Jones, A. C. Doherty, *Phys. Rev. Lett.* **98**, 140402 (2007).
- [23] M. T. Quintino, *et al.*, *Phys. Rev. A* **92**, 032107 (2015).
- [24] Q. Y. He, Q. H. Gong, M. D. Reid, *Phys. Rev. Lett.* **114**, 060402 (2015).
- [25] V. Händchen, *et al.*, *Nat Photon* **6**, 596 (2012).
- [26] P. Böhi, *et al.*, *Nat. Phys.* **5**, 592 (2009).
- [27] D. J. Wineland, J. J. Bollinger, W. M. Itano, D. J. Heinzen, *Phys. Rev. A* **50**, 67 (1994).
- [28] W. Ketterle, D. S. Durfee, D. M. Stamper-Kurn, *Bose-Einstein condensation in atomic gases, Proceedings of the International School of Physics “Enrico Fermi”, Course CXL*, M. Inguscio, S. Stringari, C. E. Wieman, eds. (IOS Press, Amsterdam, 1999), pp. 67–176.
- [29] K. Wagner, *et al.*, *J. Phys. B: At. Mol. Opt. Phys.* **47**, 225502 (2014).
- [30] G. Reinaudi, T. Lahaye, Z. Wang, D. Guéry-Odelin, *Opt. Lett.* **32**, 3143 (2007).
- [31] M. A. Joffe, W. Ketterle, A. Martin, D. E. Pritchard, *J. Opt. Soc. Am. B* **10**, 2257 (1993).

Acknowledgments

We thank M. D. Reid, P. D. Drummond, M. Oberthaler, T. Byrnes and R. Schmied for useful discussions. This work was financially supported by the Swiss National Science Foundation.

Author contributions: MF, TZ and BD performed experiments and analyzed data, supervised by PT. All authors discussed the results and contributed to the manuscript.

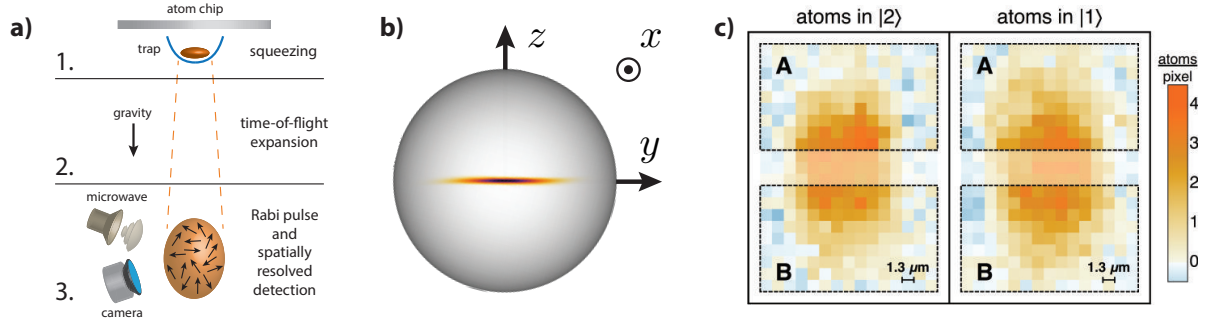


Figure 1: **Extracting entanglement from spatially separated regions of a BEC.** **a:** Experimental sequence. Step 1 consists in the preparation of a BEC in a spin squeezed state on an atom chip. In step 2 the trapping potential is switched off and the BEC expands. In step 3, a Rabi rotation pulse is applied to select the spin quadrature $\hat{S}_{\vec{n}}$ to be measured, followed by recording two high-resolution absorption images of the atomic density distributions in states $|1\rangle$ and $|2\rangle$. **b:** Illustration of the spin-squeezed state on a sphere (Wigner function, representing the quantum fluctuations of the spin) and definition of the axes \vec{n} used in the measurement of the entanglement and EPR steering criteria. **c:** Single-shot absorption images of the atomic densities in $|2\rangle$ and $|1\rangle$, showing example regions A and B used to define the collective spins \hat{S}^A and \hat{S}^B entering in the entanglement and EPR steering criteria.

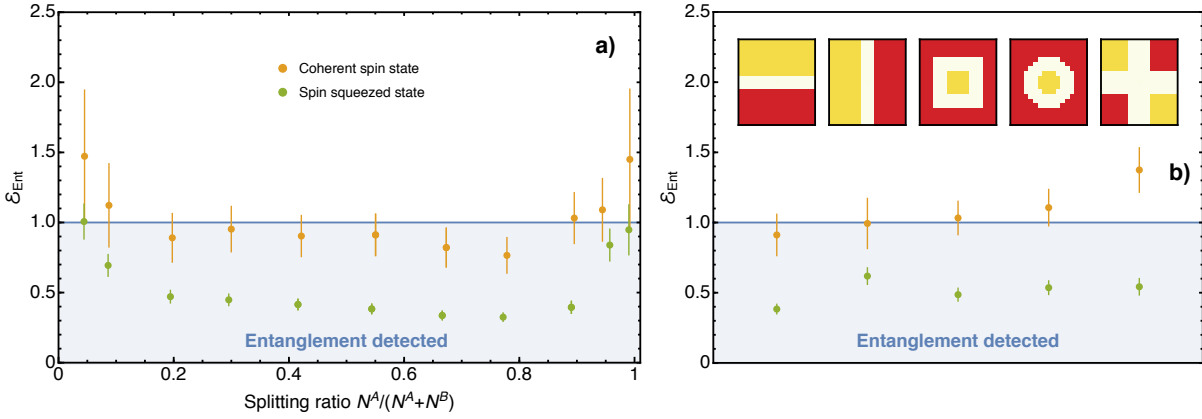


Figure 2: **Spatial entanglement patterns in the atomic cloud.** **a:** Entanglement criterion Eq. (1) evaluated for different vertical positions of the gap between regions A and B (see Fig. 1c), corresponding to different splitting ratios $N^A/(N^A + N^B)$. Data for a spin squeezed state are shown along with data for a coherent spin state. **b:** Entanglement between regions of different shapes (A =yellow, B =red). The pixel pattern used for the analysis is illustrated above the respective data points for squeezed (green) and coherent (orange) states.

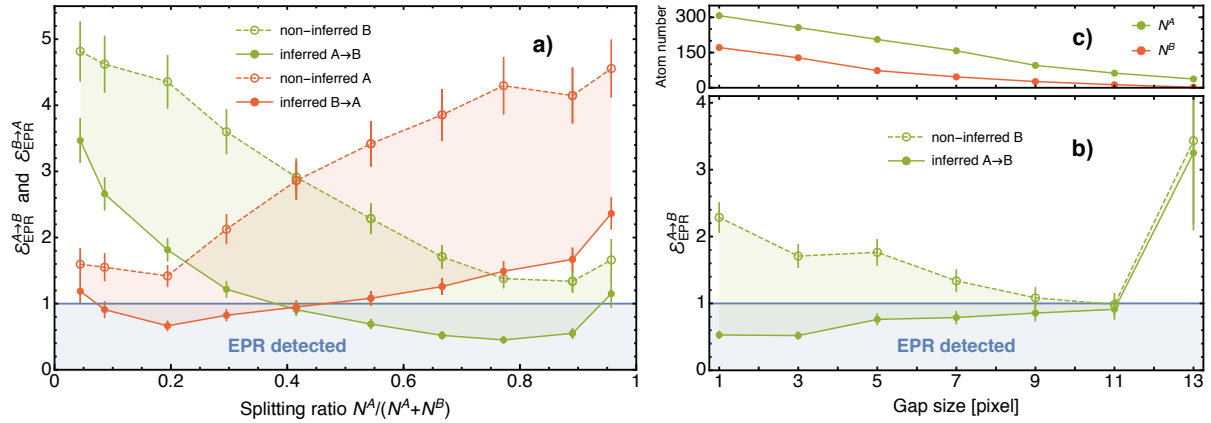


Figure 3: **Observation of Einstein-Podolsky-Rosen steering.** **a:** EPR steering criterion Eq. (2), evaluated for steering $A \rightarrow B$ (green filled circles) and $B \rightarrow A$ (red filled circles) for different vertical positions of the gap (see Fig. 1c), corresponding to different splitting ratios $N^A/(N^A + N^B)$. EPR steering is strongest for splitting ratios around 0.8 and 0.2, respectively. Empty circles: spin uncertainty relation involving the product of non-inferred variances in region B (Green) and A (Red). Lines are a guide to the eye and the shaded regions are the reduction of the uncertainty product in replacing the non-inferred variances with the inferred ones. **b:** EPR steering $A \rightarrow B$ for different widths of the gap in Fig. 1c. The center of the gap is fixed to the position showing maximum EPR steering in Fig. 3a for a width of three pixels. Even for a relatively large gap we find a significant violation of the bound, demonstrating that the correlations cannot be explained by crosstalk between the regions. Lines and shaded regions as in (a). **c:** Atom number in regions A and B as a function of the gap size.

Supplementary Materials

Imaging system and atom number calibration

Our imaging system was previously described in detail in Ref.[17, 14] and we only recall here the parameters corresponding to the present experiments. We record two absorption images, taken 1.5 ms apart, of the atomic population in the two internal states. Our detection system achieves atom number noise levels of $\sigma_{N_1,\text{det}} = 5.3$ atoms and $\sigma_{N_2,\text{det}} = 5$ atoms per whole picture. The effective scattering cross section σ_{eff} is determined with the method described by Reinaudi *et al.* [30] and we find $\sigma_{\text{eff}} = (0.68 \pm 0.02)\sigma_0$, where σ_0 is the scattering cross section of the cycling transition. Then, to take into account different detectivities for the two states, we perform Rabi oscillations with high contrast and ensure that the detected total atom number is independent of the relative population between the two states. We find that we typically have a 5 % differential detectivity in favor of state $|1\rangle$ which can be due to the different initial hyperfine sublevels. Finally, to calibrate the absolute atom number, we observe the scaling of the projection noise with the total atom number. From a coherent state equally split in $|1\rangle$ and $|2\rangle$, we look at the variance of the relative atom number. We find that the projection noise dominates our measurement as the behavior is purely linear with a fitted slope 1.031 ± 0.005 . The small deviation from unity slope is then corrected for in our analysis.

Image analysis

Due to the finite speed of the camera, the two images are taken with a delay of 1.5 ms. This means that the cloud of atoms in state $|1\rangle$ expands and falls longer than the cloud of atoms in state $|2\rangle$, leading to an increased size of $\sim 0.5\%$ (0.04 pixel) horizontally and $\sim 26\%$ (2.5 pixel) vertically (Fig. 1c), and to a center position which is $\sim 150 \mu\text{m}$ lower. Note that already after the first image the spin state of the atoms is projected. However, after the first image only atoms in $|2\rangle$ are spatially localized, while atoms in $|1\rangle$ are still completely delocalized until the second

image is taken.

After all images have been recorded, we create two binary masks, one for state $|1\rangle$ and the other for state $|2\rangle$, defining the regions A and B . Then, we evaluate the ensemble average (*i.e.* average over all images) of the two atomic densities, and use it to center the two masks. Now that the two masks are defined and positioned, we apply the same masks to all individual pictures and count the atom numbers N_1^A , N_2^A , N_1^B and N_2^B . Within the technical limitations (image resolution, blurring) discussed in the main text and in the following sections, our detection scheme realizes a projective measurement of the local collective spin in regions A and B of the expanded atomic cloud.

Optical resolution of the imaging system

To obtain an upper bound for the optical resolution of our imaging system, we image a small atomic cloud. To this end we prepare atoms in a trap which is approximately $300 \mu\text{m}$ below the chip surface, such that the atoms are trapped at a position close to where the falling atomic cloud is in the actual experiments. In this way we image the atomic cloud only $10 \mu\text{s}$ after switching off the trap, meaning that the atom density corresponds to a good approximation to the in-situ density. By using short laser pulses of $10 \mu\text{s}$ for imaging, and averaging several absorption images of this small cloud, we obtain an upper estimate of the point spread function of our optical system. Figure S1 shows the averaged absorption images, the Gaussian fit and the fit residuals. We find that the rms sizes are $\sigma_{\text{hor}} = 1.1 \text{ pixel} = 1.43 \mu\text{m}$ and $\sigma_{\text{vert}} = 1.2 \text{ pixel} = 1.56 \mu\text{m}$.

Image blurring due to random photon scattering during absorption imaging

In absorption imaging the atomic cloud is illuminated by a pulse of resonant laser light. During the pulse the atoms scatter photons, which leads to a random velocity and position during the

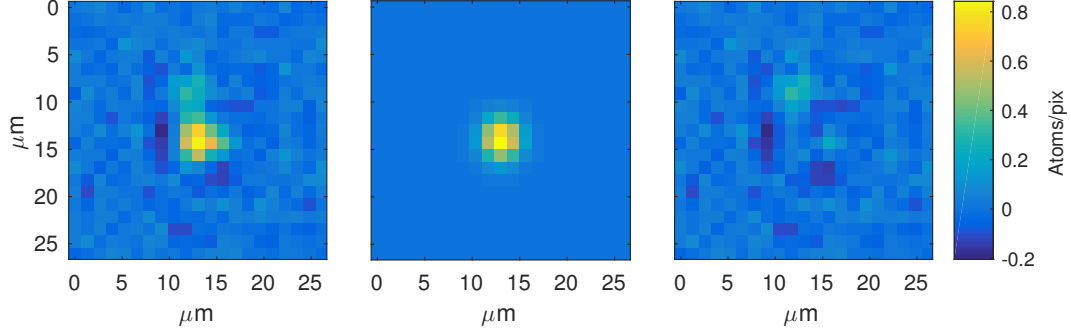


Figure S1: The left panel shows an averaged absorption image of a small atomic cloud, taken a very short time after release from the trap. The gaussian fit (center panel) gives an upper bound of the size of the optical point spread function of our imaging system. In the right panel the fit residuals are shown. The colorbar applies to all three panels.

pulse. This blurring is leading to a reduction of the effective optical resolution. In our experiment the pulse is very well described by a pulse of duration Δt_{pulse} with constant intensity. We derive here a conservative estimate of the blurring. Since the atoms are mostly scattering photons on a cycling transition, we assume here a two-level model for the atomic transition. We further assume that the light is resonant during the whole imaging pulse. These assumptions overestimate the actual spread in position, since the real scattering cross section is smaller and the scattering rate would be also reduced due to the longitudinal acceleration Doppler-shifting the atoms out of resonance during the pulse. These two effects are relatively small for our parameters, such that our estimate, although conservative, should still give reasonably good agreement with the experiment.

We are interested in the transverse spread of position due to the random scattering. As derived by Joffe *et al.* [31], the mean squared transverse position at time t is given by

$$x_{\text{rms}}^2(t) = \frac{1}{9} N_p(t) v_{\text{rec}}^2 t^2 = \frac{\Gamma}{18} \frac{s}{1+s} v_{\text{rec}}^2 t^3 .$$

Where $N_p(t)$ is the number of photons scattered between time 0 and t , and Γ and $s = \frac{I}{I_{\text{sat}}}$ are

the decay rate and saturation parameter of the transition, respectively. This size is however only giving the rms transverse size of the atomic cloud at a given time. To estimate the rms size as observed on the image, we have to time-average the spatial distribution over the pulse length. To estimate this quantity, we consider a large number M of atomic trajectories $x_j(t)$, $j = 1 \dots M$. Then, the time averaged mean squared transverse position is

$$\bar{x}_{\text{rms}}^2(\Delta t_{\text{pulse}}) = \frac{1}{M} \sum_{j=1}^M \left[\frac{1}{\Delta t_{\text{pulse}}} \int_0^{\Delta t_{\text{pulse}}} x_j(t) dt \right]^2 \leq \frac{1}{M} \sum_{j=1}^M \frac{1}{\Delta t_{\text{pulse}}} \int_0^{\Delta t_{\text{pulse}}} x_j^2(t) dt .$$

In the last expression we can exchange the order of integral and sum and use the rms transverse size at time t to estimate the expectation value of the set of trajectories. In this way we obtain

$$\bar{x}_{\text{rms}}^2(\Delta t_{\text{pulse}}) \leq \frac{1}{\Delta t_{\text{pulse}}} \int_0^{\Delta t_{\text{pulse}}} x_{\text{rms}}^2(t) dt = \frac{\Gamma}{72} \frac{s}{1+s} v_{\text{rec}}^2 (\Delta t_{\text{pulse}})^3 .$$

If we take the estimate of the size obtained from in-situ absorption images (see above) into account and the blurring due to resonant absorption during the $50 \mu\text{s}$ long imaging pulses, we obtain a total rms size of the blurred cloud on the camera of $\sigma_{\text{blur}} = 1.4 \text{ pixel} = 1.8 \mu\text{m}$. We want to emphasize here that our estimation is conservative in the sense that it gives an upper bound for the blurring, overestimating the actual effect.

Crosstalk estimation

We present here a simple model for estimating the amount of crosstalk between regions A and B . To be conservative, we consider the case of horizontal splitting which is expected to present the strongest crosstalk, due to the smaller extent of the atomic cloud in this direction. We assume the regions A and B to be described by the filter functions $f_A(x) = \Theta(x_a - x)$ and $f_B(x) = \Theta(x - x_b)$ in the horizontal x coordinate, where $\Theta(\cdot)$ is the Heaviside step function. In the vertical direction we assume the regions to extend to infinity. Note that in our case, where the atomic density is fully contained within a rectangular region on the image, this description is fully equivalent to two finite rectangular regions which are split by a gap of $x_b - x_a$. In this case,

we can reduce our model to a one dimensional problem along x , since all vertical contributions simply integrate out. For estimating the fraction of atoms which is detected in both regions due to the blurring in the images, we first calculate the effective detectivity in region A of the spin distribution in x taking the blurring into account. We model the blurring as a Gaussian with size σ_{blur} . The dedectivity in A is then given by

$$\text{det}_A(x) = \frac{1}{\sqrt{2\pi}\sigma_{\text{blur}}} \int_{-\infty}^{\infty} f_A(x') e^{-\frac{(x-x')^2}{2\sigma_{\text{blur}}^2}} dx' = \frac{1}{2} \left(1 + \text{erf} \left(\frac{x_a - x}{\sqrt{2}\sigma_{\text{blur}}} \right) \right),$$

and similar for $\text{det}_B(x)$. We estimate the atomic signal N_{AB} detected in both regions on the same image as

$$N_{AB} = \int_{-\infty}^{\infty} n(x) \text{det}_A(x) \text{det}_B(x) dx$$

where $n(x)$ is the atomic density along x . From the experimental density profile and with a gap of three pixels we get $N_{AB} < 4$ atoms, for any position of the gap.

Effect of crosstalk between regions A and B

We adopt a simple theoretical model to understand how crosstalk between regions A and B due to finite imaging resolution can result in a violation of the EPR criterion, Eq. (2). First, it is easy to check that the term $\text{Var}(g_z \hat{S}_z^A + \hat{S}_z^B)$ in Eq. (2) is minimized for the choice $g_z = -\text{Cov}(\hat{S}_z^A, \hat{S}_z^B) / \text{Var}(\hat{S}_z^A)$, which results in

$$\min_{g_z} \text{Var}(g_z \hat{S}_z^A + \hat{S}_z^B) = \text{Var}(\hat{S}_z^B) - \frac{\text{Cov}(\hat{S}_z^A, \hat{S}_z^B)^2}{\text{Var}(\hat{S}_z^A)}. \quad (3)$$

The same expression, with y instead of z , is found for the other variance in Eq. (2). Already at this point it is possible to see from Eq. (3) that, even for an uncorrelated state, if the two regions A and B are overlapping, or equivalently if some spins are attributed both to \hat{S}^A and \hat{S}^B , the resulting covariance will be non-zero. This reduces $\text{Var}(g_{\vec{n}} \hat{S}_{\vec{n}}^A + \hat{S}_{\vec{n}}^B)$, for any measurement quadrature \vec{n} , and leads to a violation of the inequality in Eq. (2).

We make a quantitative estimate of this violation originating from crosstalk in the following minimal example. Consider N spins $1/2$, and the associated collective spin operators

$$\hat{S}^A = \sum_{i=1}^l \hat{s}^{(i)} \quad \text{and} \quad \hat{S}^B = \sum_{i=k}^N \hat{s}^{(i)}, \quad (4)$$

where $\hat{s}^{(i)}$ is the spin operator acting on the i -th spin. If $l \geq k$, then $n = l - k + 1$ spins contribute both to \hat{S}^A and \hat{S}^B . Under the assumption of uncorrelated spins, each prepared in state $(|\uparrow\rangle + |\downarrow\rangle)/\sqrt{2}$, we observe that

$$\text{Cov}(\hat{S}_z^A, \hat{S}_z^B) = \text{Var}\left(\sum_{i=k}^l s_z^{(i)}\right) = \frac{n}{4}, \quad (5)$$

which results in

$$\min_{\{g_y, g_z\}} \mathcal{E}_{\text{EPR}}^{A \rightarrow B} = 4 \left((N^B/4) - \frac{(n/4)^2}{(N^A/4)} \right)^2 / (N^B/2)^2 = 1 - \frac{2n^2}{N^B(N - N^B)} + \mathcal{O}(n^3), \quad (6)$$

where $N^A = l$ and $N^B = N - k + 1$ are the number of spins in the two regions. From Eq. (6) we conclude that a coherent state can violate the EPR criterion Eq. (2) if there is a crosstalk of n spins. For our regions A and B as defined in Fig. 1, we estimate $n = N_{AB} = 4$, which yields $\min_{\{g_y, g_z\}} \mathcal{E}_{\text{EPR}}^{A \rightarrow B} = 0.998$ for a coherent state.